Crystalline phase engineering on cocatalysts: A promising approach to enhancement on photocatalytic conversion of carbon dioxide to fuels

Fan Ye[a,1], Fang Wang[a,1], Chenchen Meng[a], Lijie Bai[a], Junying Li[a], Pingxing Xing[a], Botao Teng[a,**], Leihong Zhao[a,**], Song Bai[a,b,*]

[a] *Key Laboratory of the Ministry of Education for Advanced Catalysis Materials, College of Chemistry and Life Sciences, Zhejiang Normal University, Jinhua, Zhejiang, 321004, PR China*
[b] *Hefei National Laboratory for Physical Sciences at the Microscale, School of Chemistry and Materials Science, University of Science and Technology of China, Hefei, Anhui, 230026, PR China*

A R T I C L E   I N F O

A B S T R A C T

Photocatalytic conversion of CO_2 to value-added fuels, a promising route to address the depletion of fossil fuels and concomitant global warming, can be improved by cocatalysts through promoting the electron-hole separation and offering catalytic active sites for the surface reactions. However, the enhancement of the photocatalytic performance is greatly determined by the surface and interface structures of cocatalysts. Herein, for the first time, we demonstrate that the photocatalytic activity in the CO_2 reduction can be optimized through crystalline phase design of cocatalysts. In this work, Ru nanocrystals in face-centered cubic (fcc) and hexagonal close-packed (hcp) phases are *in-situ* grown on C_3N_4 nanosheets to form different C_3N_4-Ru hybrid structures, respectively. It was found that the hcp Ru achieved higher average CO and CH_4 production rate but lower H_2 production rate in comparison with fcc Ru. As revealed by the experimental characterizations combined with theory simulations, the phase-dependent photocatalytic performance is resulted from the different surface reaction behaviors on the fcc and hcp Ru cocatalysts. The adsorption energy of CO_2 molecules on the dominated $(10\bar{1}1)$ face of hcp Ru is higher than that on the dominated (111) face of fcc Ru. As a result, the stronger interaction between CO_2 molecules and the surface of hcp Ru contributes to the enhanced photocatalytic activity and selectivity of C_3N_4-hcp Ru in reduction of CO_2. This work highlights the importance in the crystalline phase engineering in cocatalyst for enhanced CO_2 photoreduction.

1. Introduction

To address the increasing energy and environmental related concerns, production of chemical fuels utilizing renewable solar energy has received extensive attention [1–3]. Particularly, photocatalytic conversion of CO_2 to value-added chemicals, such as methane $(CO_2 + 8H^+ + 8e^- \rightarrow CH_4 + 2H_2O)$ and carbon oxide $(CO_2 + 2H^+ + 2e^- \rightarrow CO + H_2O)$ is of particular interest because of its capability of mimicking natural photosynthesis through a green and renewable route [4–11]. Nowadays, a variety of semiconductor based photocatalysts such as TiO_2 [12,13], C_3N_4 [14], CdS [15], CeO_2 [16], Zn_2GeO_4 [17], $ZnGa_2O_4$ [18] and $BiWO_6$ [19] have been studied for CO_2 reduction reaction. However, the major challenges so far in the technology of photocatalytic CO_2 reduction are serious electron-hole recombination in bulk semiconductor photocatalysts and low adsorption and activation abilities of stable CO_2 molecules on semiconductor surface [20]. In view of this restriction, metal and alloy cocatalysts, such as Pd [21], Pt [22,23], Ag [24], Rh [25], AuCu [26], and PtCu [27], were loaded on the semiconductor surface for enhanced photocatalytic CO_2 conversion efficiency. On one hand, metal cocatalysts trap the photogenerated electrons from semiconductor in promoting the electron-hole separation. On the other hand, the surface of cocatalysts offers highly reactive sites in promoting the adsorption and activation of CO_2 molecules [28]. Graphitic-phase carbon nitride (g-C_3N_4), a typical visible light-excitable n-type polymeric semiconductor was widely used as the cocatalyst supporter in the photocatalytic CO_2 reduction reaction [29–31]. The large surface area of C_3N_4 nanosheets facilitates the loading of cocatalyst, while the low thickness shortens the electron

---

transfer distance to the cocatalysts and reduces the possibility of electrons loss. In addition, the conjugated aromatic structure of C_3N_4 offers manifold coupling configurations with cocatalysts, ensuring a strong connection between them for high-efficient interfacial electron transfer [14].

In spite of the efforts, the photocatalytic activity and selectivity of semiconductor supported metal cocatalyst hybrid structures in CO_2 reduction reaction is still far from practical applications. For instance, resulted from the high H_2O activation ability on the surface of cocatalysts, the reduction of H_2O to H_2 ($2H^+ + 2e^- \rightarrow H_2$) is a preferential or competitive process, which lowers the product yields and selectivity [32]. Considering the two key roles of cocatalysts in the photocatalytic process, surface and interface design of cocatalysts is a promising route to further enhance the photocatalytic activity and selectivity in CO_2 reduction [33–35]. Generally, it is believed that the design of cocatalysts with high electron trapping ability from semiconductor and abundant surface active sites for the adsorption and activation of CO_2 molecules is vital to realize high-performance photocatalysis. On the other hand, the adsorption and activation abilities of H_2O molecules on the surface of designed cocatalysts should be reduced to decrease the side reaction.

In the surface and interface design of cocatalysts in photocatalysis, crystallographic structure, namely the arrangement of atoms in the nanocrystals, is an important parameter. On one hand, crystallographic structure plays a critical role in influencing the electronic band structure of cocatalyst. Thus the electron trapping ability of cocatalyst from light-harvesting semiconductor is greatly dependent on its crystallographic phase [36,37]. On the other hand, different crystallographic structures result in different atomic arrangements on the surface of cocatalyst. Thus reactive sites in different types and densities are exposed on the surface of cocatalysts for catalytic reaction [38,39]. Herein, for the first time, we demonstrate that the photocatalytic performance in CO_2 reduction reaction can be optimized through crystalline phase engineering on metal cocatalysts. In this paper, ruthenium (Ru) nanocrystals in face-centered cubic (fcc) and hexagonal close-packed (hcp) phases are *in-situ* grown on C_3N_4 nanosheets to form C_3N_4-fcc Ru and C_3N_4-hcp Ru semiconductor-cocatalyst hybrid structures, respectively. Based on the experimental results and theoretical simulations, it is found that though fcc Ru and hcp Ru possess the comparable electron trapping ability from C_3N_4, the surface of hcp Ru cocatalyst exhibits superior surface adsorption and activation abilities of CO_2 molecules in comparison with that of fcc Ru. Futhermore, a lower surface catalytic ability in reduction of H_2O to H_2 is realized by hcp Ru. As a result, the as-obtained C_3N_4-hcp Ru exhibits significantly superior photocatalytic activity and selectivity in conversion of CO_2 to fuels as compared with C_3N_4-fcc Ru.

2. Experimental

2.1. Chemicals

Ru(acac)$_3$ (Aladdin, R118502), RuCl$_3$·nH$_2$O (Aladdin, R109234), triethylene glycol (TEG, Aladdin, T110409) and ethylene glycol (EG, Sigma-Aldrich, 324558) were used in our synthesis. All other chemicals were of analytical grade and purchased from Sinopharm Chemical Reagent Co., Ltd. without further purification. The water used in all experiments was de-ionized.

2.2. Synthesis of C_3N_4 nanosheets

Bulk g-C_3N_4 was synthesized through a modified method according to previous reports [27,40]. In a typical synthesis, 20 g of urea was dissolved in 10 mL water. The obtained solution was heated at 550 °C for 3 h (0.5 °C/min ramp rate; natural cooling). Then the resultant yellow agglomerates were milled into g-C_3N_4 powder in a mortar. Then the as-synthesized g-C_3N_4 powder was further dispersed in TEG and EG

to form the corresponding suspension of C_3N_4 nanosheets (15 mg/mL) with probe sonication for 1 h, respectively.

2.3. Synthesis of C_3N_4-Ru samples

In a typical synthesis of C_3N_4-fcc Ru, 0.21 mmol of Ru(acac)$_3$ and 0.5 mmol of Poly(vinyl pyrrolidone) (PVP, K30, monomer units) were dissolved in 10 mL of TEG suspension of C_3N_4 at room temperature. The dispersion was then heated to 200 °C and maintained at this temperature for 3 h. After completion of the reaction, the resultant product was separated by centrifugation, washed with water three times, and dried at 45 °C in vacuum. In the synthesis of C_3N_4-hcp Ru, 0.21 mmol of RuCl$_3$·nH$_2$O and 0.5 mmol of PVP were dissolved in 10 mL of EG suspension of C_3N_4 at room temperature. The dispersion was then heated to 200 °C and maintained at this temperature for 3 h. The as-obtained product was separated by centrifugation, washed with water three times, and dried at 45 °C in vacuum.

2.4. Sample characterizations

X-ray powder diffraction (XRD) patterns were recorded by using a Philips X'Pert Pro Super X-ray diffractometer with Cu-Kα radiation (λ = 1.54178 Å). X-ray photoelectron spectra (XPS) were collected on an ESCALab 250 X-ray photoelectron spectrometer, using non-monochromatized Al-Kα X-ray as the excitation source. Transmission electron microscopy (TEM) and high-resolution TEM (HRTEM) were taken on a JEOL JEM-2100F field-emission high-resolution transmission electron microscope operated at 200 kV. The concentrations of metal elements were measured as follows: the samples were dissolved with a mixture of HNO_3 and HCl (1:3, volume ratio), which was then diluted with 1% HNO_3. The concentrations of metal ions were then measured through a Thermo Scientific PlasmaQuad 3 inductively-coupled plasma mass spectrometry (ICP-MS). The loading amounts of Ru on the C_3N_4 nanosheets were determined by sample weighing prior to the dissolution of Ru for the ICP-MS measurements. UV–vis-NIR diffuse reflectance data were measured in the spectral region of 200–800 nm with a Shimadzu SolidSpec-3700 spectrophotometer. Photoluminescence (PL) spectra were carried out on a HITACHI F-7000 Spectrofluorometer with the excitation wavelength of 390 nm. Fourier transform infrared (FTIR) measurements were performed on a Nicolet 8700 FTIR spectrometer in a KBr pellet, scanning from 4000 to 500 cm^{-1}. The electron spin resonance (ESR) spectra were characterized with a JES-FA200 electron spin resonance spectrometer by mixing the sample with 5,5-dimethyl-1-pyrroline-N-oxide (DMPO) (100 μL, 50 mM) in water under Xe lamp irradiation.

2.5. Photoelectrochemical measurements

3.0-mg as-synthesized products were dispersed in a mixture of 10-μL nafion and 10-μL ethanol, which were then uniformly spin-dropped onto a 1 cm × 1 cm indium tin oxide (ITO)-coated glass. Subsequently, the ITO-coated glass was heated at 80 °C for 1 h in a vacuum oven. The photocurrents were measured on a CHI 760E electrochemical station (Shanghai Chenhua, China) under irradiation of a 300-W Xe lamp (Solaredge 700, China). Visible light (780 nm > λ > 420 nm) was used as the illumination source, which was realized by using both a 420-nm cutoff filter (long-wave-pass) and a 780-nm cutoff filter (short-wave-pass). The power density of visible light was measured to be 100 mW cm^{-2}. Standard three-electrode setup was used with the ITO coated glass as photoelectrode, a Pt foil as counter electrode, and an Ag/AgCl electrode as reference electrode. Three electrodes were inserted in a quartz cell filled with 0.5-M Na_2SO_4 electrolyte. The photoresponse of as-prepared photoelectrodes (i.e., *I-t*) was operated by measuring the photocurrent densities under chopped light irradiation (light on/off cycles: 60 s) at a bias potential of 0.2 V *vs.* Ag/AgCl for 400 s. The electrochemical impedance spectroscopy (EIS) was carried
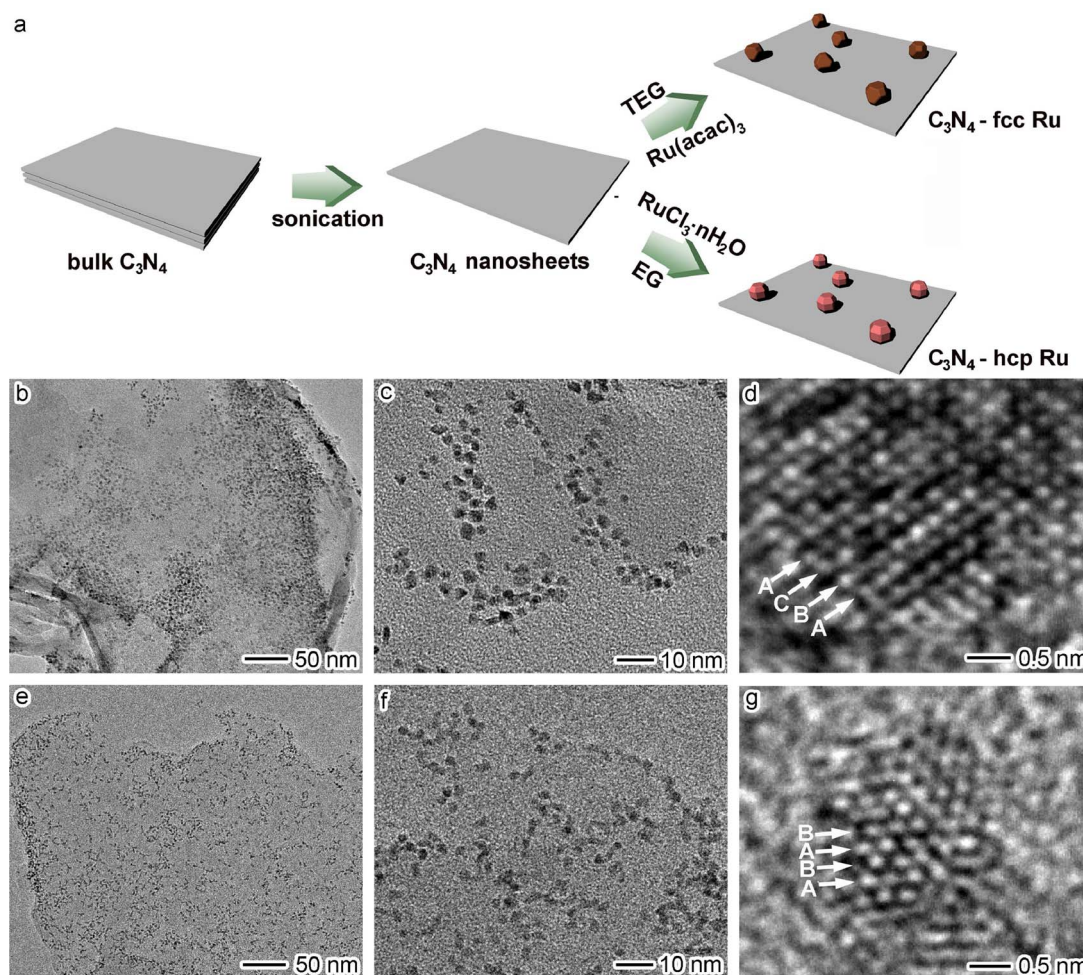
Fig. 1. (a) Schematic illustrating the synthesis of C_3N_4-fcc Ru and C_3N_4-hcp Ru; (b–d) TEM (b and c) and HRTEM (d) images of C_3N_4-fcc Ru; (e–g) TEM (e and f) and HRTEM (g) images of C_3N_4-hcp Ru.

out in the frequency range of 10^{-1}–10^5 Hz with an AC voltage amplitude of 10 mV at a bias potential of 0.2 V *vs.* Ag/AgCl.

2.6. Photocatalytic CO_2 reduction measurements

CO_2 photocatalytic reduction reaction was typically conducted in a 100 mL reactor purchased from Beijing Perfect Light Company (China). To remove possible trace organic contaminants, all the samples were treated at 200 °C for 5 h in air. In a typical measurement, 15 mg of photocatalyst was dispersed on the flat glass plate on the bottom of the reactor. And 2 mL H_2O was added and surrounded the plate. The reactor loaded with catalysts was first purged with high purity CO_2 for 30 min. Then the light-irradiation experiment was performed by using a 300 W Xe lamp with visible light as the illumination source. The power density of visible light (780 nm > λ > 420 nm) was measured to be 100 mW cm^{-2}. The photocatalytic reaction was typically performed for 4 h. During the irradiation, 1 mL gas was sampled from the glass chamber at a given time interval(1 h). The amount of products evolved were determined using gas chromatography (GC-2014, Shimadzu) with Ar as carrier gas. The H_2 and O_2 were determined using a thermal conductivity detector (TCD). The CH_4 were measured by flame ionization detector (FID) and the CO was converted to CH_4 by a methanation reactor and then analyzed by the FID. During the stability test, the photocatalysts were collected after each run and then reused for photoreduction of CO_2.

2.7. Computational methods

The theoretical works were calculated by the Cambridge Sequential Total Energy Package (CASTEP) in Materials Studio Package [41,42]. The ultrasoft pseudopotential with a frozen-core approximation was adopted for the electron-ion interaction [43]. The generalized gradient approximation (GGA) [44] was used for the electronic exchange and correlation. The Perdew-Burke-Ernzerhof functional was used in this work [45]. The Kohn-Sham one-electron states were expanded in a plane wave basis. The cutoff energy and smearing value were set as 400 and 0.1 eV, respectively. Brillouin zone integration was approximated by a sum over special k-points using the Monkhorst–Pack method [46]. The energy convergence criterion was set to 2.0×10^{-6} eV/atom; while the maximum force and displacement tolerances of structure optimization were set to 0.05 eV/Å and 5×10^{-3} Å, respectively [47].

The calculated lattice constants of hcp Ru are 2.720 and 4.284 Å, which are well consistent with the experimental value, 2.706 and 4.282 Å, respectively. The fcc lattice constant is 3.807 Å, which is also agreement with the experimental one, 3.830 Å. According to the simulation of fcc and hcp Ru nanoparticles [39], the possible exposed surfaces of the fcc Ru(111), (100), (221), (211), (311), (110), (210), (310), (321) and (320), as well as the hcp Ru(0001), (110), (10$\bar{1}$2), (111), (201), (10$\bar{1}$0), (10$\bar{1}$1) and (21$\bar{3}$0) were used for the investigation of CO_2 adsorption behaviors. The vacuum space was set as 12 Å between the slabs to minimize their interaction. Free CO_2 was optimized in a cubic lattice with the length of 15 Å [48].

CO_2 adsorption behaviors at different sites on substrate were

systematically studied, and the corresponding adsorption energy was defined as:

$$E_{ads} = E_{CO2/substrate} - (E_{CO2} + E_{substrate}) \qquad (1)$$

where $E_{CO2/substrate}$ is the total energy of the substrate with CO_2; E_{CO2} and $E_{substrate}$ are the energies of free CO_2 and substrate, respectively [27]. Therefore, a negative value means exothermic adsorption, while a positive one means endothermic adsorption. The more negative the adsorption energy, the stronger the adsorption [49].

3. Results and discussion

3.1. Sample synthesis and characterization

In the typical synthesis of the samples, bulk C_3N_4 was firstly prepared with urea as precursor (Fig. S1), which was then exfoliated into C_3N_4 nanosheets via a sonication treatment (Fig. 1a) [27,40]. As shown in Fig. S2, the exfoliated C_3N_4 nanosheets are in wrinkles with micrometer-sized surface and nanoscale thickness. In the design of the hybrid photocatalysts, C_3N_4 as light harvesting semiconductor can be excited by visible light and produce photogenerated electron-hole pairs, in which electrons can transfer to the surface of metal cocatalysts for CO_2 reduction reaction through the formation of Schottky junction [28].

In the second step, Ru nanocrystals in fcc phase were then *in situ* grown on the flat surface of C_3N_4 nanosheets through reducing Ru (acac)$_3$ with TEG acting as both the reducing agent and solvent, while hcp Ru nanocrystals were *in situ* grown on C_3N_4 nanosheets with $RuCl_3 \cdot nH_2O$ as Ru source as well as EG as reducing agent and solvent (Fig. 1a) [50]. As shown in the TEM images (Fig. 1b and e), Ru nanocrystals were uniformly distributed over the flat surface of C_3N_4 nanosheets in both the samples without any agglomerations. The Ru nanocrystals are in narrow size distribution and the average sizes of them are determined to be 3.7 and 3.0 nm in C_3N_4-fcc Ru and C_3N_4-hcp Ru samples, respectively (Figs. 1c and f, S3). HRTEM image in the C_3N_4-fcc Ru clearly reveals the fcc ABCABCABC... stacking sequence in the monocrystalline Ru nanocrystals, while a hcp ABABAB... stacking sequence is observed in the HRTEM image of Ru nanocrystals in the C_3N_4-hcp Ru sample (Fig. 1d and g), indicating the different crystalline phases of Ru cocatalysts between the two samples.

The crystal structures of the as-obtained C_3N_4 based samples were further revealed by X-ray powder diffraction (XRD) pattern (Fig. 2a). For bare C_3N_4, weak (100) peak at 13.1° represents the in-planar repeating tri-*s*-triazine unit, while the strong (002) peak at 27.4° is the characteristic interlayer stacking refection of the conjugated aromatic segments [51]. As for the XRD pattern of C_3N_4-fcc Ru, additional peaks are in good agreement with the fcc Ru (JCPDS No. 88-2333). In contrast, additional peaks in the XRD pattern of C_3N_4-hcp Ru sample are indexed to the hcp Ru (JCPDS No. 06-0663). The XRD results confirm the combination of C_3N_4 with Ru in different phases in the two samples. It should be noted that there is a slight shift of the XRD peaks of C_3N_4-hcp Ru to smaller angles compared with the JCPDS data with the possible reason of some lattice distortions in the hcp Ru nanoparticles. The chemical structures of the samples were further indicated by Fourier transform infrared (FTIR) spectra (Fig. 2b). It can be clearly seen that the all the characteristic peaks, including the N–H stretching (3000–3600 cm^{-1}), stretching vibrations of CN heterocycles (1000–1800 cm^{-1}) and breathing mode of the triazine units (810 cm^{-1}), are observed in the spectra of bare C_3N_4 [52]. In comparison with the FTIR spectrum of bare C_3N_4, no additional peak was shown in the spectra of C_3N_4-Ru samples, suggesting that there is no obvious change of C_3N_4 during the further growth of Ru nanocrystals. The compositions of the as-obtained C_3N_4-Ru samples were further determined by X-ray photoelectron spectra (XPS). As shown in Fig. 2c, the survey XPS spectrum of C_3N_4-fcc Ru indicates the existence of C, N and Ru elements. The C1s high-resolution spectrum can be deconvolved

into two peaks at 284.6 and 288.0 eV, which are assigned to the graphitic carbon (C–C) and sp^2-bonded aromatic structure (N–C=N), respectively (Fig. 2d) [53]. In the high-resolution XPS spectrum of N1s (Fig. 2e), the binding energies at 398.4, 400.2, and 404.1 eV correspond to the sp^2-hybridized aromatic N (C=N–C), tertiary N bonded to carbon atoms [N-(C)$_3$] and π-excitations, respectively [54]. As for the high-resolution Ru3p spectrum (Fig. 2f), the doublet centered at 461.0 and 483.2 eV are assigned to the Ru3p$_{3/2}$ and Ru3p$_{1/2}$ of Ru (0), revealing the metallic Ru in the C_3N_4-fcc Ru sample [55]. The XPS spectra of C_3N_4-hcp Ru are much similar to those of C_3N_4-fcc Ru, confirming the same chemical composition of the two C_3N_4-Ru samples (Fig. S4). In facilitating the comparison of following photocatalytic performance, the loading amounts of Ru on the C_3N_4 were kept the same in the two samples, which was confirmed by the inductively coupled plasma mass spectrometry (ICP-MS) measurement (Table S1).

3.2. Charge kinetics and photocatalytic performance analysis

Considering the photocatalytic activity is greatly determined by the generation and transfer of photo-induced charge carriers, the charge kinetics behaviors of the C_3N_4 based samples were investigated prior to the photocatalytic performance analysis. The light absorption capabilities of the samples were first revealed by UV–vis-NIR diffuse reflectance spectra. As shown in Fig. 3a, bare C_3N_4 exhibits a light absorption in visible region with an adsorption edge at *ca.* 460 nm. In comparison bare C_3N_4, the C_3N_4-Ru samples exhibit additional light absorption at longer wavelengths, which is resulted from the excitation of bound electrons to high energy levels through interband transitions of non-plasmonic Ru [56,57]. More importantly, the two C_3N_4-Ru samples exhibit similar light absorption properties in visible region, revealing their comparable abilities in generating electron-hole pairs under visible light irradiation. Then the electron-hole separation abilities of the samples were further analyzed by the photocurrent response under visible light irradiation. As shown in Fig. 3b, the photocurrent of C_3N_4 is much lower than those of C_3N_4-Ru samples, indicating that Ru nanocrystals as cocatalysts can trap the photogenerated electrons from C_3N_4 in promoting the electron-hole separation. The smooth charge transfer between the electron donor of C_3N_4 and electron acceptor of Ru elucidates the strong metal-semiconductor interaction between them. More importantly, C_3N_4-fcc Ru and C_3N_4-hcp Ru display approximate photocurrent response, suggesting the similar electron trapping abilities of Ru cocatalysts in different phases. This statement is further confirmed by the EIS (Fig. 3c), in which C_3N_4-fcc Ru and C_3N_4-hcp Ru show approximative arc radii, revealing the similar resistance owing to the equivalent interfacial electron transfer ability from C_3N_4 to Ru in different phases. Furthermore, the information of electron-hole separation can also be provided by PL emission spectra. Under the excitation wavelength of 390 nm, C_3N_4 exhibits a PL emission with the maximum at 460 nm, which is quenched in almost the same degree by fcc and hcp Ru cocatalysts (Fig. 3d). In view of the PL of semiconductor is induced by the radiative electron-hole recombination, the similar PL quench degree reflects that the fcc and hcp Ru cocatalysts have approximate electron trapping abilities in suppressing the electron-hole recombination in C_3N_4 [58].

Have confirmed the charge kinetics of the C_3N_4 based samples, their photocatalytic performance in the reduction of CO_2 with H_2O was further investigated. The samples were excited under visible light irradiation in the mixed vapor of CO_2 and H_2O, and the amounts of products were determined by gas chromatography. As shown in Fig. 4a, bare C_3N_4 produces H_2, CO and CH_4, indicating that the photogenerated electrons participate in both the conversion of CO_2 to CO and CH_4, and the reduction of H_2O to H_2. According to the required electrons to generate reduction products using the following equation:

$$\text{Selectivity} \quad (\%) = [8\nu(CH_4) + 2\nu(CO)]/[2\nu(CO) + 8\nu(CH_4) + 2\nu(H_2)] \times 100\% \qquad (2)$$

Fig. 2. (a) XRD patterns and (b) FTIR spectra of C_3N_4, C_3N_4-fcc Ru and C_3N_4-hcp Ru; (c–f) XPS spectra of C_3N_4-fcc Ru: (c) survey spectrum; (d) C1s; (e) N1s and (f) Ru3p high-resolution spectra.

the selectivity of C_3N_4 in CO_2 reduction is evaluated to be 38.5%. When the Ru nanocrystals are loaded on the light-harvesting C_3N_4, the average production rates of H_2, CO and CH_4 significantly increase, confirming the cocatalyst role of Ru in the photocatalytic process. More importantly, 4.78 $\mu mol\,g_{cat}^{-1}\,h^{-1}$ of average CO production rate and 0.78 $\mu mol\,g_{cat}^{-1}\,h^{-1}$ of average CH_4 production rate are achieved by C_3N_4-hcp Ru, 1.6 and 2.3 times higher than those of C_3N_4-fcc Ru, respectively. Furthermore, it is interesting that the average H_2 evolution rate of C_3N_4-hcp Ru is lower than that of C_3N_4-fcc Ru. As a result, the photocatalytic selectivity in CO_2 reduction increases from 46.5% of C_3N_4-fcc Ru to 71.8% of C_3N_4-hcp Ru, revealing that more electrons generated in C_3N_4-hcp Ru participate in the photocatalytic CO_2 reduction reaction. In addition to the high photocatalytic activity and selectivity, the C_3N_4-hcp Ru also exhibits excellent stability in the CO_2 reduction reaction. There are only slight declines in the average production rate of CO and CH_4 during the four cyclic processes, which may be resulted from the loss of photocatalysts during the collection of them after each run and reused for the next cycle as well as the fall off of minimal Ru nanocrystals from C_3N_4 nanosheets during the cycles. Moreover, the photocatalytic selectivity in CO_2 reduction maintains in the range of 70%–72.2%. From the TEM image of the sample after the cyclic process (Fig. S5), it can be clearly seen that most of Ru

nanocrystals are still firmly attached to the flat surface of C_3N_4 nanosheets without any aggregation. Only a trace amount of Ru nanocrystals are detached from the C_3N_4 nanosheets. Also in the XRD patterns and XPS spectra of C_3N_4-hcp Ru before and after the cycles, it can be seen that there is no obvious change in the spectra after the cycles except the slight decrease in the intensities of Ru peaks (Fig. S6). In spite of this, it was found that the photocatalysts can be repeated for more than 15 times (60 h). The high photocatalytic activity of C_3N_4-hcp Ru is also confirmed by the superior CO and CH_4 production rate and higher selectivity in CO_2 reduction in comparison with previous reported C_3N_4 supported fcc metal cocatalyst structures, further showing the importance of crystalline phase of cocatalysts in the photocatalytic reaction (Table S2) [14,29,59–61]. It should be noted that the formation of O_2 over the C_3N_4 based samples was also confirmed by us, indicating that the photogenerated holes left in the C_3N_4 also participate in the H_2O oxidation reaction ($2H_2O + 4h^+ \rightarrow O_2 + 4H^+$). The generation of holes in the reaction is also confirmed by ESR spectra (Fig. S7), in which ESR signals with intensity ratio of 1:2:2:1 are clearly displayed after mixing the C_3N_4-hcp Ru with DMPO in water under visible light irradiation, suggesting that the holes participate in the production of hydroxyl radicals (OH) [62,63]. Given the equivalent abilities of the two C_3N_4-Ru samples in generating and transferring
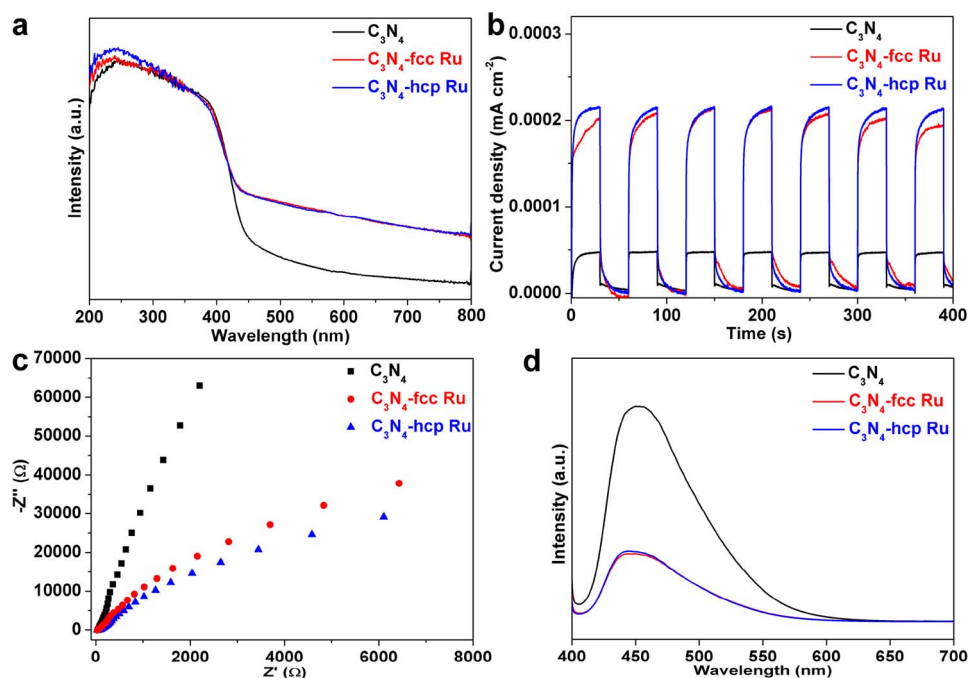
Fig. 3. (a) UV–vis-NIR diffuse reflectance spectra of C_3N_4, C_3N_4-fcc Ru and C_3N_4-hcp Ru; (b and c) photocurrent *vs.* time (I-t) curves (b) and EIS Nyquist plots (c) of C_3N_4, C_3N_4-fcc Ru and C_3N_4-hcp Ru at 0.2 V *vs.* Ag/AgCl under visible light (780 nm > λ > 420 nm) irradiation; (d) PL spectra of C_3N_4, C_3N_4-fcc Ru and C_3N_4-hcp Ru excited at 390 nm.
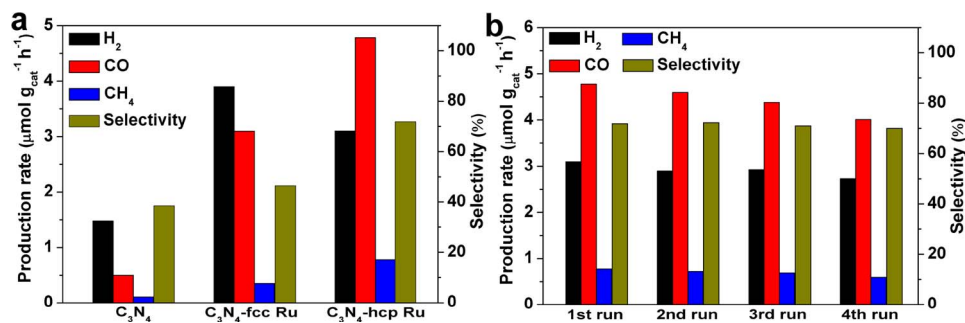

Fig. 4. (a) Average H_2, CO and CH_4 evolution rates of C_3N_4, C_3N_4-fcc Ru and C_3N_4-hcp Ru photocatalysts as well as their selectivities in CO_2 reduction under visible light (420 < λ < 780 nm) irradiation; (b) average H_2, CO and CH_4 evolution rates of C_3N_4-hcp Ru photocatalyst as well as its selectivity in CO_2 reduction in four successive cycles under visible light (420 < λ < 780 nm) irradiation.
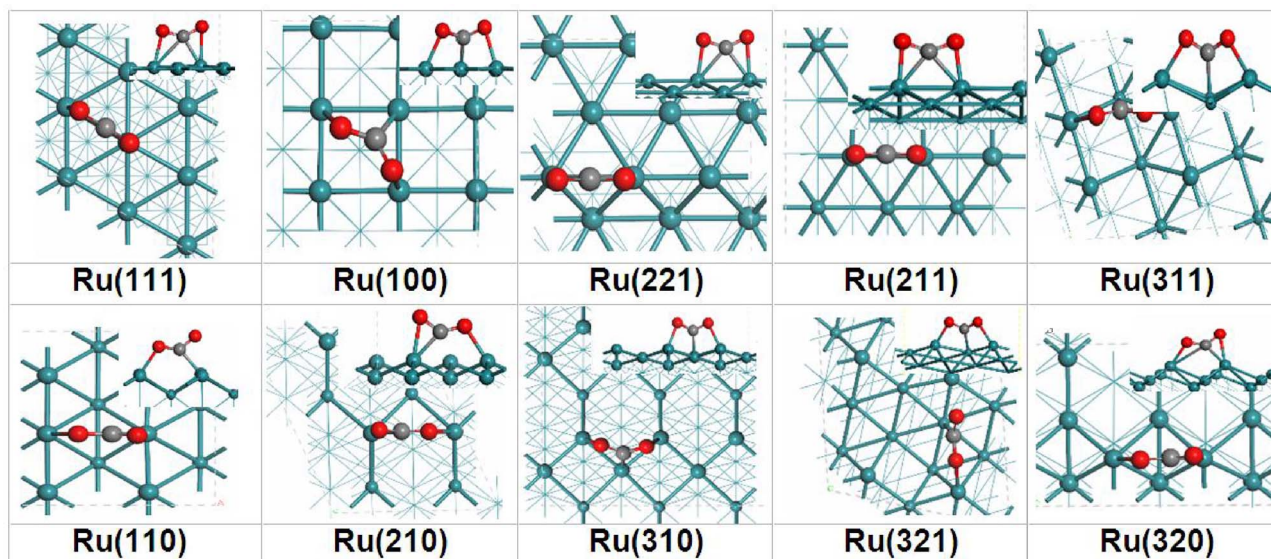

Fig. 5. Most stable configurations of CO_2 on fcc Ru surfaces (blue-green, dark and red ones for Ru, C and O atoms, respectively). (For interpretation of the references to colour in this figure legend, the reader is referred to the web version of this article.)

Table 1
Parameters of CO_2 on the fcc Ru surfaces.

Surface	Coordination number	Work function/ eV	E_{ads}/eV	d_{C-O}/Å		Mulliken charge
111	9	4.63	−0.12	1.252	1.262	−0.50
100	8	4.63	−0.66	1.257	1.258	−0.53
221	7	4.13	−0.84	1.257	1.260	−0.59
211	7	4.07	−0.75	1.259	1.264	−0.59
311	7	4.03	−1.24	1.293	1.297	−0.64
110	7	3.96	−0.62	1.255	1.280	−0.59
210	6	4.10	−1.01	1.268	1.276	−0.61
310	6	4.02	−1.38	1.298	1.321	−0.70
321	6	3.94	−1.27	1.294	1.298	−0.65
320	6	3.84	−1.15	1.260	1.281	−0.61

Table 2
Parameters of CO_2 on the hcp Ru surfaces.

Surface	Coordination number	Work function/ eV	E_{ads}/eV	d_{C-O}/Å		Mulliken charge
0001	9	4.33	−0.12	1.251	1.256	−0.50
11$\bar{2}$0	7	4.09	−1.30	1.294	1.296	−0.67
10$\bar{1}$2	7(8)	4.08	−0.93	1.261	1.268	−0.59
	7(9)	4.15	−0.70	1.261	1.261	−0.60
11$\bar{2}$1	6	3.95	−1.40	1.292	1.295	−0.67
20$\bar{2}$1	6	3.93	−1.13	1.262	1.266	−0.64
	8	4.05	−0.33	1.249	1.264	−0.52
10$\bar{1}$0	6	3.69	−0.98	1.267	1.271	−0.64
	8	4.38	−0.58	1.303	1.330	−0.53
10$\bar{1}$1	6	3.66	−1.05	1.267	1.269	−0.65
	8	4.38	−0.39	1.256	1.258	−0.53
21$\bar{3}$0	5	3.93	−1.41	1.298	1.299	−0.69
	7	4.03	−1.00	1.244	1.285	−0.61

photo-induced electrons, the different photocatalytic performance may be resulted from the different reaction behaviors on the surface of Ru cocatalysts in different phases, which gives a good explanation of higher CO and CH_4 average production rates but lower H_2 production rate of C_3N_4-hcp Ru as compared with those of C_3N_4-fcc Ru.

3.3. Photocatalytic mechanism analysis

To further analyze the possible mechanism of the phase-dependent photocatalytic performance in CO_2 reduction reaction, theoretical simulation was carried out by density functional theory (DFT) calculation. The adsorption behaviors of CO_2 on the surfaces of the fcc and hcp Ru nanoparticles were systematically investigated. The most stable configurations of CO_2 on the fcc surfaces were shown in Fig. 5 and the corresponding parameters were listed in Table 1, while the configurations on the hcp surfaces and the corresponding parameters were shown in Fig. 6 and Table 2, respectively. It can be found that the interactions between the surfaces of Ru cocatalysts with CO_2 molecules are highly

related with the coordination number and the atom arrangement of surface Ru atoms. For both the fcc and hcp Ru, it can be found that the interaction energies between CO_2 and Ru surfaces increase with the reduction of the coordination number [64]. With the high coordination number of 9, fcc Ru(111) and hcp Ru(0001) surfaces exhibit the same CO_2 adsorption energy (−0.12 eV). When the coordination number decreases to 8, the adsorption energy of CO_2 is −0.66 eV on fcc Ru(100) and −0.39 eV on hcp Ru(10$\bar{1}$1). The values further decrease to −1.30 to −0.62 eV on the surface of 7-coordinated Ru and −1.40 to −0.98 eV on the face of 6-coordinated Ru. Furthermore, the work function is also dependent on the atomic arrangement of Ru. Generally, lower coordination number of Ru contributes to a smaller work function. Though both the adsorption energy and work function are affected by the facet of Ru, the differences between the work functions are much smaller in comparison with those between the CO_2 adsorption energy.
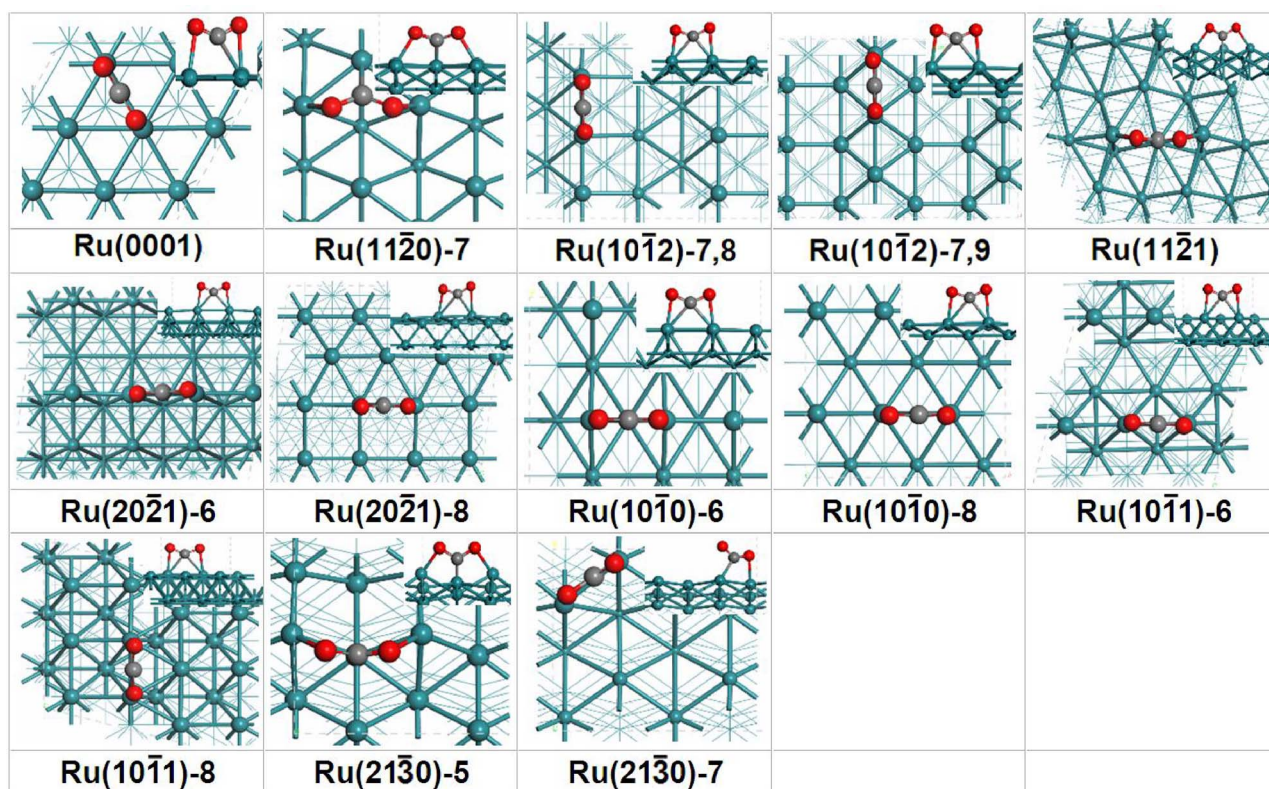

Fig. 6. Most stable configurations of CO_2 on hcp Ru surfaces. Number after the surface index indicates the coordination number of surface Ru atom (blue-green, dark and red ones for Ru, C and O atoms, respectively). (For interpretation of the references to colour in this figure legend, the reader is referred to the web version of this article.)
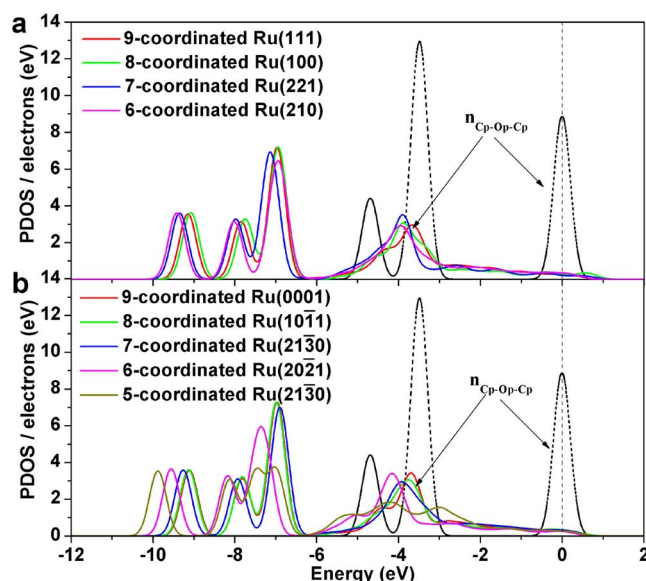
Fig. 7. PDOS of CO_2 on the typical (a) fcc and (b) hcp Ru surfaces with different surface Ru coordination numbers. Short dash curve is for free CO_2 molecule, straight line is for the Fermi level.

This conclusion is further supported by the partial density of states of CO_2 adsorbed on Ru surfaces. As shown in Fig. 7, the HOMO and LUMO orbitals of free CO_2 are the $n_{Cp-Op-Cp}$ and $\pi^*_{Cp-Op-Cp}$, respectively. With the adsorption of CO_2 molecules on the surface of Ru, its electronic peak shifts towards lower energy due to the interactions between CO_2 and Ru surfaces. The peak area of HOMO orbital of CO_2 decreases compared with that of free molecule, and the LUMO orbital of CO_2 shifts downward to the Fermi energy level. These results indicate that CO_2 loses electrons to Ru surface and the electrons on Ru surfaces feedback to CO_2 simultaneously. Furthermore, it can be seen that the peak shifts increase with the decrease of Ru coordination number. This indicates the interactions between CO_2 and Ru surfaces increase with the reduction of coordination number of Ru, which is in consistent with the results reported in the literature [65,66].

According to previous reported literature [39], based on Wulff construction from DFT calculated surface energies, fcc Ru is octahedron-like populated mainly by close-packed (111) facets, while hcp Ru is a dihedral-like shape dominated with (0001) and (10$\bar{1}$1) surface (Fig. S8). Though the adsorption energies of CO_2 on fcc Ru(111) and hcp Ru (0001) are almost the same (-0.12 eV), the adsorption energy of CO_2 on the hcp Ru(10$\bar{1}$1) (-0.39 eV) is much higher than that on fcc Ru (111) (-0.12 eV). As a result, stronger interaction occurs between CO_2 molecules and hcp Ru(10$\bar{1}$1), which is further supported by the higher negative Mulliken charges of adsorbed CO_2. The Mulliken charges are $-0.50\,e^-$ on fcc Ru(111) and $-0.53\,e^-$ on hcp Ru(10$\bar{1}$1), respectively (Tables 1 and 2). Furthermore, there are more edges and corners with low coordination atoms in the hcp Ru nanocrystals as compared with those in the fcc ones [39]. Considering the lower coordination number of Ru results in higher CO_2 adsorption energy, the higher densities of edges and corners in hcp Ru are potential active sites for CO_2 conversion. Therefore, the higher surface adsorption ability of CO_2 as well as the higher density of active sites in the edges and corners contributes to the higher photocatalytic activity of the hcp Ru in reduction of CO_2, which is well consistent with the experimental results. It should be noted that the work function of fcc Ru(111) is 4.63 eV, much similar to those of hcp Ru(0001) (4.33 eV) and Ru(10$\bar{1}$1) (4.38 eV), suggesting the approximate electron trapping ability of Ru cocatalysts from C_3N_4 with lower work function (4.31 eV) despite the different phases [14]. This result is in good agreement with the nearly identical probability of interfacial electron transfer from C_3N_4 to fcc and hcp Ru, further indicating the charge transfer behavior is not affected by altering the

crystalline phases of Ru cocatalysts. Thus the phase-dependent photocatalytic performance in reduction of CO_2 mainly attributes to the different interactions between CO_2 and the surface of Ru cocatalysts.

4. Conclusions

In summary, crystalline phase engineering was performed on the Ru cocatalysts for enhanced photocatalytic performance in the conversion of CO_2 into fuels. Ru cocatalysts in fcc and hcp phases acting as cocatalysts were deposited on the flat surface of C_3N_4 nanosheets, respectively. It turns out that the hcp Ru cocatalysts realize the superior average CO and CH_4 production rate but lower H_2 production rate in comparison with fcc Ru. As a result, the selectivity of C_3N_4-fcc Ru in CO_2 reduction is significantly higher than that of C_3N_4-hcp Ru (71.8% versus 46.5%). It was found that the phase-dependent photocatalytic performance is not resulted from the varied electron transfer abilities from C_3N_4 to Ru, but the different surface reaction kinetics on the surface of fcc and hcp Ru cocatalysts. Theoretical simulations indicate that the CO_2 adsorption energy on the dominated (10$\bar{1}$1) face of hcp Ru is higher than that on the dominated (111) face of fcc Ru. Thus the stronger interaction between CO_2 molecules and surface of hcp Ru cocatalysts contributes to the enhanced photocatalytic activity and selectivity of C_3N_4-hcp Ru. This work presents an important advancement towards the design of cocatalysts for enhanced photocatalytic performance through crystalline phase engineering.

Acknowledgments

Appendix A. Supplementary data

Supplementary material related to this article can be found, in the online version, at doi:https://doi.org/10.1016/j.apcatb.2018.02.046.

References

[1] A.L. Linsebigler, G. Lu, J.T. Yates Jr, Photocatalysis on TiO_2 surfaces: principles, mechanisms, and selected results, Chem. Rev. 95 (1995) 735–758.
[2] A. Fujishima, K. Honda, Electrochemical photolysis of water at a semiconductor electrode, Nature 238 (1972) 37–38.
[3] X. Chen, S. Shen, L. Guo, S.S. Mao, Semiconductor-based photocatalytic hydrogen generation, Chem. Rev. 110 (2010) 6503–6570.
[4] W. Tu, Y. Zou, Z.G. Zhou, Photocatalytic conversion of CO_2 into renewable hydrocarbon fuels: state-of-the-art accomplishment, challenges, and prospects, Adv. Mater. 26 (2014) 4607–4626.
[5] S.N. Habisreutinger, L. Schmidt-Mende, J.K. Stolarczyk, Photocatalytic reduction of CO_2 on TiO_2 and other semiconductors, Angew. Chem. Int. Ed. 52 (2013) 7372–7408.
[6] A. Dhakshinamoorthy, S. Navalon, A. Corma, H. Garcia, Photocatalytic CO_2 reduction by TiO_2 and related titanium containing solids, Energy Environ. Sci. 5 (2012) 9217–9233.
[7] K. Jabbour, P. Massiani, A. Davidson, S. Casale, N.E. Hassan, Ordered mesoporous "one-pot" synthesized Ni-Mg(Ca)-Al_2O_3 as effective and remarkably stable catalysts for combined steam and dry reforming of methane (CSDRM), Appl. Catal. B: Environ. 201 (2017) 527–542.
[8] Y. Cao, M. Lu, J. Fang, L. Shi, D. Zhang, Hexagonal boron nitride supported meso SiO_2-confined Ni catalysts for dry reforming of methane, Chem. Commun. 53 (2017) 7549–7552.
[9] X. Zhao, H. Li, J. Zhang, L. Shi, D. Zhang, Design and synthesis of NiCe@m-SiO_2 yolk-shell framework catalysts with improved coke- and sintering-resistance in dry reforming of methane, Int. J. Hydrogen Energy 41 (2016) 2447–2456.
[10] P.V. Tuza, M.M.V.M. Souza, Steam reforming of methane over catalyst derived from ordered double perovskite: effect of crystalline phase transformation, Catal. Lett. 146 (2016) 47–53.
[11] D. Zhang, X. Du, L. Shi, R. Gao, Shape-controlled synthesis and catalytic application of ceria nanomaterials, Dalton Trans. 41 (2012) 14455–14475.
[12] J. Yu, J. Low, W. Xiao, P. Zhou, M. Jaroniec, Enhanced photocatalytic CO_2-reduction activity of anatase TiO_2 by coexposed {001} and {101} facets, J. Am. Chem. Soc. 136 (2014) 8839–8842.
[13] C. Dong, M. Xing, J. Zhang, Economic hydrophobicity triggering of CO_2 photoreduction for selective CH_4 generation on noble-metal-free TiO_2-SiO_2, J. Phys.

Chem. Lett. 7 (2016) 2962–2966.

[14] S. Bai, X. Wang, C. Hu, M. Xie, J. Jiang, Y. Xiong, Two-dimensional g-C$_3$N$_4$: an ideal platform for examining facet selectivity of metal co-catalysts in photocatalysis, Chem. Commun. 50 (2014) 6094–6097.

[15] J. Yu, J. Jian, B. Cheng, M. Jaroniec, A noble metal-free reduced graphene oxide–CdS nanorod composite for the enhanced visible-light photocatalytic reduction of CO$_2$ to solar fuel, J. Mater. Chem. A 2 (2014) 3407–3416.

[16] P. Li, Y. Zhou, Z. Zhao, Q. Xu, X. Wang, M. Miao, Z. Zou, Hexahedron prism-anchored octahedronal CeO$_2$: crystal facet-based homojunction promoting efficient solar fuel synthesis, J. Am. Chem. Soc. 137 (2015) 9547–9550.

[17] Q. Liu, Y. Zhou, J. Kou, X. Chen, Z. Tian, J. Gao, S. Yan, Z. Zou, High-yield synthesis of ultralong and ultrathin Zn$_2$GeO$_4$ nanoribbons toward improved photocatalytic reduction of CO$_2$ into renewable hydrocarbon fuel, J. Am. Chem. Soc. 132 (2010) 14385–14387.

[18] S.C. Yan, S. Ouyang, J. Gao, M. Yang, J.Y. Feng, X.X. Fan, L.J. Wan, Z.S. Li, J.H. Ye, Y. Zhou, Z.G. Zou, A room-temperature reactive-template route to mesoporous ZnGa$_2$O$_4$ with improved photocatalytic activity in reduction of CO$_2$, Angew. Chem. Int. Ed. 49 (2010) 6400–6404.

[19] H. Cheng, B. Huang, Y. Liu, Z. Wang, X. Qin, X. Zhang, Y. Dai, An anion exchange approach to Bi$_2$WO$_6$ hollow microspheres with efficient visible light photocatalytic reduction of CO$_2$ to methanol, Chem. Commun. 48 (2012) 9729–9731.

[20] S. Bai, J. Jiang, Q. Zhang, Y. Xiong, Steering charge kinetics in photocatalysis: intersection of materials syntheses, characterization techniques and theoretical simulations, Chem. Soc. Rev. 44 (2015) 2893–2939.

[21] Y. Zhu, Z. Xu, W. Jiang, S. Zhong, L. Zhao, S. Bai, Engineering on the edge of Pd nanosheet cocatalysts for enhanced photocatalytic reduction of CO$_2$ to fuels, J. Mater. Chem. A 5 (2017) 2619–2628.

[22] W.N. Wang, W.J. An, B. Ramalingam, S. Mukherjee, D.M. Niedzwiedzki, S. Gangopadhyay, P. Biswas, Size and structure matter: enhanced CO$_2$ photoreduction efficiency by size-resolved ultrafine Pt nanoparticles on TiO$_2$ single crystals, J. Am. Chem. Soc. 134 (2012) 11276–11281.

[23] C. Dong, M. Xing, J. Zhang, Double-cocatalysts promote charge separation efficiency in CO$_2$ photoreduction: spatial location matters, Mater. Horiz. 3 (2016) 608–612.

[24] K. Iizuka, T. Wato, Y. Miseki, K. Saito, A. Kudo, Photocatalytic reduction of carbon dioxide over Ag cocatalyst-loaded ALa$_4$Ti$_4$O$_{15}$(A = Ca, Sr, and Ba) using water as a reducing reagent, J. Am. Chem. Soc. 133 (2011) 20863–20868.

[25] Y. Zhu, Z. Xu, Q. Lang, W. Jiang, Q. Yin, S. Zhong, S. Bai, Grain boundary engineered metal nanowire cocatalysts for enhanced photocatalytic reduction of carbon dioxide, Appl. Catal. B: Environ. 206 (2017) 282–292.

[26] S. Neaţu, J.A. Macia-Agullo, P. Concepcion, H. Garcia, Gold–copper nanoalloys supported on TiO$_2$ as photocatalysts for CO$_2$ reduction by water, J. Am. Chem. Soc. 136 (2014) 15969–15976.

[27] Q. Lang, Y. Yang, Y. Zhu, W. Hu, W. Jiang, S. Zhong, P. Gong, B. Teng, L. Zhao, S. Bai, High-index facet engineering of PtCu cocatalysts for superior photocatalytic reduction of CO$_2$ to CH$_4$, J. Mater. Chem. A 5 (2017) 6686–6694.

[28] J. Yang, D. Wang, H. Han, C. Li, Roles of cocatalysts in photocatalysis and photoelectrocatalysis, Acc. Chem. Res. 46 (2013) 1900–1909.

[29] Q. Lang, W. Hu, P. Zhou, T. Huang, S. Zhong, L. Yang, J. Chen, S. Bai, Twin defects engineered Pd cocatalyst on C$_3$N$_4$ for enhanced photocatalytic performance in CO$_2$ reduction reaction, Nanotechnology 28 (2017) 484003.

[30] W. Yu, D. Xu, T. Peng, Enhanced photocatalytic activity of g-C$_3$N$_4$ for selective CO$_2$ reduction to CH$_3$OH via facile coupling of ZnO: a direct Z-scheme mechanism, J. Mater. Chem. A 3 (2015) 19936–19947.

[31] J. Fu, B. Zhu, C. Jiang, B. Cheng, W. You, J. Yu, Hierarchical porous O-doped g-C$_3$N$_4$ with enhanced photocatalytic CO$_2$ reduction activity, Small 13 (2017) 1603938.

[32] Y. Zhu, C. Gao, S. Bai, S. Chen, R. Long, L. Song, Z. Li, Y. Xiong, Hydriding Pd cocatalysts: an approach to giant enhancement on photocatalytic CO$_2$ reduction into CH$_4$, Nano Res. 10 (2017) 3396–3406.

[33] S. Bai, W. Yin, L. Wang, Z. Li, Y. Xiong, Surface and interface design in cocatalysts for photocatalytic water splitting and CO$_2$ reduction, RSC Adv. 6 (2016) 57446–57463.

[34] S. Bai, Y. Xiong, Some recent developments in surface and interface design for photocatalytic and electrocatalytic hybrid structures, Chem. Commun. 51 (2015) 10261–10271.

[35] S. Bai, W. Jiang, Z. Li, Y. Xiong, Surface and interface engineering in photocatalysis, ChemMedChem 1 (2015) 223–239.

[36] S. Bai, L. Wang, X. Chen, J. Du, Y. Xiong, Chemically exfoliated metallic MoS$_2$ nanosheets: a promising supporting co-catalyst for enhancing the photocatalytic performance of TiO$_2$ nanocrystals, Nano Res. 8 (2015) 175–183.

[37] L. Kornblum, P. Shekhter, Y. Slovatizky, Y. Amouyal, M. Eizenberg, Composition and crystallography dependence of the work function: experiment and calculations of Pt-Al alloys, Phys. Rev. B 86 (2012) 125305.

[38] J.X. Liu, H.Y. Su, D.P. Sun, B.Y. Zhang, W.X. Li, Crystallographic dependence of CO activation on cobalt catalysts: HCP versus FCC, J. Am. Chem. Soc. 135 (2013) 16284–16287.

[39] W.Z. Li, J.X. Liu, J. Gu, W. Zhou, S.Y. Yao, R. Si, Y. Guo, H.Y. Su, C.H. Yan, W.X. Li, Y.W. Zhang, D. Ma, Chemical insights into the design and development of face-centered cubic ruthenium catalysts for Fischer–Tropsch synthesis, J. Am. Chem. Soc. 139 (2017) 2267–2276.

[40] Z. Wang, W. Guan, Y. Sun, F. Dong, Y. Zhou, W.K. Ho, Water-assisted production of honeycomb-like g-C$_3$N$_4$ with ultralong carrier lifetime and outstanding photocatalytic activity, Nanoscale 7 (2015) 2471–2479.

[41] V. Milman, B. Winkler, J.A. White, C.J. Pickard, M.C. Payne, E.V. Akhmatskaya, R.H. Nobes, Electronic structure, properties, and phase stability of inorganic crystals: a pseudopotential plane-wave study, Int. J. Quantum Chem. 77 (2000) 895–910.

[42] M.D. Segall, P.J.D. Lindan, M.J. Probert, C.J. Pickard, P.J. Hasnip, S.J. Clark, M.C. Payne, First-principles simulation: ideas, illustrations and the CASTEP code, J. Phys.: Condens. Matter 14 (2002) 2717–2744.

[43] D. Vanderbilt, Soft self-consistent pseudopotentials in a generalized eigenvalue formalism, Phys. Rev. B 41 (1990) 7892–7895.

[44] M.C. Payne, M.P. Teter, D.C. Allan, T.A. Arias, J.D. Joannopoulos, Iterative minimization techniques for ab initio total-energy calculations: molecular dynamics and conjugate gradients, Rev. Mod. Phys. 64 (1992) 1045–1097.

[45] J.P. Perdew, Y. Wang, Accurate and simple analytic representation of the electrongas correlation energy, Phys. Rev. B 45 (1992) 13244–13249.

[46] H.J. Monkhorst, J.D. Pack, Special points for brillouin-zone integrations, Phys. Rev. B 13 (1976) 5188–5192.

[47] Y.J. Yang, B.T. Teng, Y. Liu, X.D. Wen, Crotonaldehyde adsorption on Ir(111), an interesting trans- and cis-configuration transformation, Appl. Surf. Sci. 357 (2015) 369–375.

[48] K.J. Zhu, F. Wang, B.T. Teng, X.D. Wen, M. Fan, X.N. Liu, A new insight into the theoretical design of highly dispersed and stable ceria supported metal nanoparticles, J. Colloid Interface Sci. 513 (2018) 775–783.

[49] X.D. Yao, K.J. Zhu, B.T. Teng, C.M. Yu, Y.L. Zhang, Y. Liu, M. Fan, X.D. Wen, Effects of strong interactions between Ti and ceria on the structures of Ti/CeO$_2$, Phys. Chem. Chem. Phys. 18 (2016) 32494–32502.

[50] K. Kusada, H. Kobayashi, T. Yamamoto, S. Matsumura, N. Sumi, K. Sato, K. Nagaoka, Y. Kubota, H. Kitagawa, Discovery of face-centered-cubic ruthenium nanoparticles: facile size-controlled synthesis using the chemical reduction method, J. Am. Chem. Soc. 135 (2013) 5493–5496.

[51] X. Wang, K. Maeda, A. Thomas, K. Takanabe, G. Xin, J.M. Carlsson, K. Domen, M. Antonietti, A metal-free polymeric photocatalyst for hydrogen production from water under visible light, Nat. Mater. 8 (2009) 76–80.

[52] H. Xu, J. Yan, X. She, L. Xu, J. Xia, Y. Xu, Y. Song, L. Huang, H. Li, Grapheneanalogue carbon nitride: novel exfoliation synthesis and its application in photocatalysis and photoelectrochemical selective detection of trace amount of Cu^{2+}, Nanoscale 6 (2014) 1406–1415.

[53] J. Mao, T. Peng, X. Zhang, K. Li, L. Ye, L. Zan, Effect of graphitic carbon nitride microstructures on the activity and selectivity of photocatalytic CO$_2$ reduction under visible light, Catal. Sci. Technol. 3 (2013) 1253–1260.

[54] W. Yin, L. Bai, Y. Zhu, S. Zhong, L. Zhao, Z. Li, S. Bai, Embedding metal in the interface of p-n heterojunction with stack design for superior Z-scheme photocatalytic hydrogen evolution, ACS Appl. Mater. Interfaces 8 (2016) 23133–23142.

[55] C. Liu, K.S. Kim, J. Baek, Y. Cho, S. Han, S.W. Kim, N.K. Min, Y. Choi, J.U. Kim, C.J. Lee, Improved field emission properties of double-walled carbon nanotubes decorated with Ru nanoparticles, Carbon 47 (2009) 1158–1164.

[56] H. Sakamoto, T. Ohara, N. Yasumoto, Y. Shiraishi, S. Ichikawa, S. Tanaka, T. Hirai, Hot-electron-induced highly efficient O$_2$ activation by Pt nanoparticles supported on Ta$_2$O$_5$ driven by visible light, J. Am. Chem. Soc. 137 (2015) 9324–9332.

[57] S. Sarina, H.Y. Zhu, Q. Xiao, E. Jaatinen, J. Jia, Y. Huang, Z. Zheng, H. Wu, Viable photocatalysts under solar-spectrum irradiation: nonplasmonic metal nanoparticles, Angew. Chem. Int. Ed. 53 (2014) 2935–2940.

[58] S. Bai, J. Ge, L. Wang, M. Gong, M. Deng, Q. Kong, L. Song, J. Jiang, Q. Zhang, Y. Luo, Y. Xie, Y. Xiong, A unique semiconductor-metal-graphene stack design to harness charge flow for photocatalysis, Adv. Mater. 26 (2014) 5689–5695.

[59] S. Cao, Y. Li, B. Zhu, M. Jaroniec, J. Yu, Facet effect of Pd cocatalyst on photocatalytic CO$_2$ reduction over g-C$_3$N$_4$, J. Catal. 349 (2017) 208–217.

[60] Z. Ni, F. Dong, H. Huang, Y. Zhang, New insights into how Pd nanoparticles influence the photocatalytic oxidation and reduction ability of g-C$_3$N$_4$ nanosheets, Catal. Sci. Technol. 6 (2016) 6448–6458.

[61] J. Yu, K. Wang, W. Xiao, B. Cheng, Photocatalytic reduction of CO$_2$ into hydrocarbon solar fuels over g-C$_3$N$_4$–Pt nanocomposite photocatalysts, Phys. Chem. Chem. Phys. 16 (2014) 11492–11501.

[62] F. Zhang, X. Li, Q. Zhao, D. Zhang, Rational design of ZnFe$_2$O4/In$_2$O$_3$ nanoheterostructures: efficient photocatalyst for gaseous 1,2-dichlorobenzene degradation and mechanistic insight, ACS Sustain. Chem. Eng. 4 (2016) 4554–4562.

[63] J. Sun, X. Li, Q. Zhao, M.O. Tade, S. Liu, Construction of p-n heterojunction β-Bi$_2$O$_3$/BiVO$_4$ nanocomposite with improved photoinduced charge transfer property and enhanced activity in degradation of ortho-dichlorobenzene, Appl. Catal. B: Environ. 219 (2017) 259–268.

[64] G. Ouyang, K.J. Zhu, L. Zhang, P.F. Cui, B.T. Teng, X.D. Wen, Effects of coordination number of Au catalyst on oxygen species and their catalytic roles, Appl. Surf. Sci. 387 (2016) 875–881.

[65] B.T. Teng, Y. Zhao, F.M. Wu, X.D. Wen, Q.P. Chen, W.X. Huang, A density functional theory study of CF$_3$CH$_2$I adsorption and reaction on Ag(111), Surf. Sci. 606 (2012) 1227–1232.

[66] B.T. Teng, W.X. Huang, F.M. Wu, Y.Z. Lan, D.B. Cao, A density functional theory study of the CH$_2$I$_2$ reaction on Ag(111): thermodynamics, kinetics, and electronic structures, J. Chem. Phys. 132 (2010) 024715.